NIST Special Publication 260-185

Method for measuring the diameter of polystyrene latex reference spheres by atomic force microscopy

John A. Dagata
Natalia Farkas
Prem Kavuri
Andras E. Vladàr
Chung-Lin Wu
Hiroshi Itoh
Kensei Ehara

This publication is available free of charge from:
http://dx.doi.org/10.6028/NIST.SP.260-185

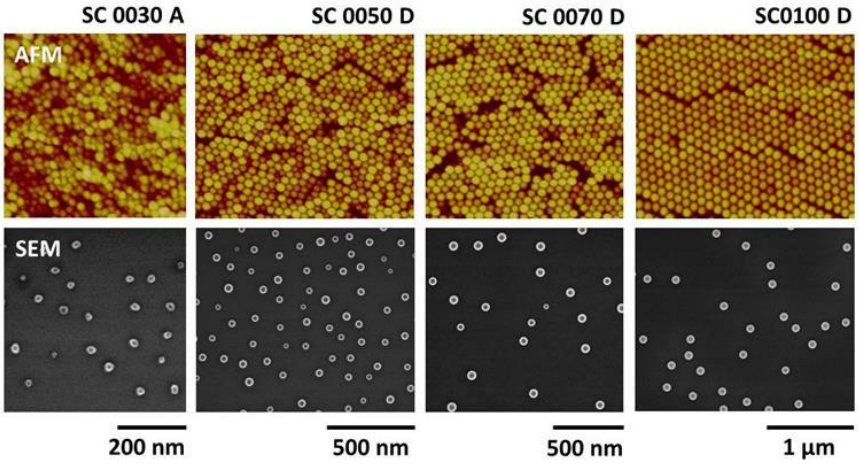

National Institute of Standards and Technology
U.S. Department of Commerce

NIST Special Publication 260-185

Method for measuring the diameter of polystyrene latex reference spheres by atomic force microscopy

John A. Dagata
Natalia Farkas
Prem Kavuri
Andras E. Vladàr
Engineering Physics Division
Physical Measurement Laboratory

Chung-Lin Wu
Center for Measurement Standards, ITRI
Hsinchu, Taiwan

Hiroshi Itoh
Kensei Ehara
National Metrology Institute of Japan
Tsukuba, Japan

This publication is available free of charge from:
http://dx.doi.org/10.6028/NIST.SP.260-185

July 2016

U.S. Department of Commerce
Penny Pritzker, Secretary

National Institute of Standards and Technology
Willie May, Under Secretary of Commerce for Standards and Technology and Director

National Institute of Standards and Technology Special Publication SP 260-185
Natl. Inst. Stand. Technol. Spec. Publ. 260-185, 26 pages (July 2016)
CODEN: NSPUE2

This publication is available free of charge from: http://dx.doi.org/10.6028/NIST.SP.260-185

ABSTRACT

This report presents a correlated height and width measurement model for particle size analysis of spherical particles by atomic force microscopy (AFM). It is complementary to more familiar methods based on a single value of the particle height or on a line average obtained from a close-packed particle array. Significant influence quantities affecting the determination of average particle size and its uncertainty are considered for the important case of polystyrene latex (PSL) reference materials. Particle-substrate deformation, resulting from adhesive contact between particle and substrate during sample preparation, is estimated as a function of particle size. Post-processing of AFM datasets is explored as a means of eliminating bias due to non-steady state measurement conditions. These biases arise from variable particle-tip interaction caused by drift of instrumental parameters from their optimal settings during long acquisition times and inevitable wear of the AFM probe. Changes of the initial probe shape are established using a Si/SiO_2 multilayer tip characterizer and are updated periodically during the analysis of sequential data sets for combinations of several particles sizes and different probes. Finally, the capability of this procedure to serve as a statistical error-correction scheme in AFM particle-size metrology is assessed.

KEY WORDS

Atomic force microscopy
Nanoparticle diameter
Polystyrene
Standard Reference Material

TABLE OF CONTENTS

LIST OF TABLES

LIST OF FIGURES

1. Introduction

Polystyrene latex (PSL) spheres represent an important historical and still very relevant class of reference materials (RMs) for particle sizing. A chief feature is that they are relatively inexpensive to manufacture, available in a wide variety of diameters, approach nearly ideal properties of sphericity, monodispersity, material homogeneity, and can be readily functionalized for specialized applications or intended use in metrological, environmental, and biomedical investigations [1-3]. Atomic force microscope (AFM) is one of several instruments capable of providing nanometer scale measurements and is under active development as a primary calibration instrument in a number of national measurement laboratories [4] as well as being an accessible user's tool for routine size characterization.

The possibility that PSL spheres might be compressible has been explored recently by Garnaes [5] and it was suggested that particle deformation encountered in AFM height and raft measurements may arise from several possible sources: Adhesive contact forces between the particle and substrate during sample preparation, δ_{PS}, and imaging-induced deformation of the particles by the AFM probe tip, δ_{PT}, may affect the height measurement. While it is possible to measure an overall height deformation, $\Delta h = \delta_{PS} + \delta_{PT}$, it is not possible to estimate these terms and their uncertainties separately without additional information or assumptions. Width measurements made on rafts may be subject to deformation due to particle-particle interactions, δ_{PP}, during lattice formation in the sample preparation stage. An additional concern is lattice imperfections or air gaps, δ_{AG}. Again, raft measurements yield an overall deformation, $\Delta w = \delta_{PP} + \delta_{AG}$, and do not permit estimates of these potential contributions to be determined separately.

In order to estimate uncertainties for these parameters, various assumptions about the nature of the interactions have been made, leading to sometimes inconsistent conclusions. For instance, Misumi et al. [6] were able to obtain an effective Young's modulus from an *elastic* contact mechanics model for 30 nm and 100 nm PSL particles by assuming that δ_{PT} is insignificant compared with δ_{PS}. On the other hand, work by He et al. [7], based on extrapolation of high loading force data and other contact mechanics models, suggested that δ_{PT} is inevitable and *plastic* deformation may be significant after all.

In this report we propose an alternative to height and raft measurements based on the analysis of correlated AFM height and width data of individual PSL spheres. Immediately, the problem simplifies because $\Delta w = 0$ for individual particles so we need only focus on the deconvolution of Δh in the uncertainty analysis. The trade-off is that AFM probe geometry now enters the measurement process explicitly, thus requiring separate evaluation. In the present article, we demonstrate that sufficient information about the AFM probe geometry is available by the appropriate use of a tip characterizer to make this extra effort worthwhile.

2. Measurand and measurement model

Odin et al. [8] discussed how to estimate particle size on the basis of the simple geometric measurement model. Its elements consist of a sphere resting on a flat substrate and a conical AFM probe tip. All interactions are treated as purely repulsive. Simulations for individual particles and particle rafts for a variety of probe types were presented in that work. The calculation may be summarized briefly as follows: An AFM tip of radius, R_{tip}, and full cone angle, α, moves along the x axis, and it encounters a spherical particle of radius R. The cross section generated by the Odin interaction model is marked by closed circles in Fig. 1a. The problem is rendered dimensionless by use of the parameter $\lambda = R_{tip}/R$. Then, the apparent width of the particle is given by

$$\Delta L = 2 \cdot \Delta L_{1/2} \tag{1}$$

where

$$\Delta L_{1/2} = \frac{(1+\lambda)+(1-\lambda)\cdot\sin(\alpha/2)}{\cos(\alpha/2)} \quad (2)$$

and the apparent height is given by

$$z_o = \frac{(1+\lambda)+(1-\lambda)\cdot\sin(\alpha/2)}{\sin(\alpha/2)} \pm \frac{x_o}{\tan(\alpha/2)} \quad (3)$$

evaluated at the point at which it reaches its maximum value, i.e., $x_o = 0$.

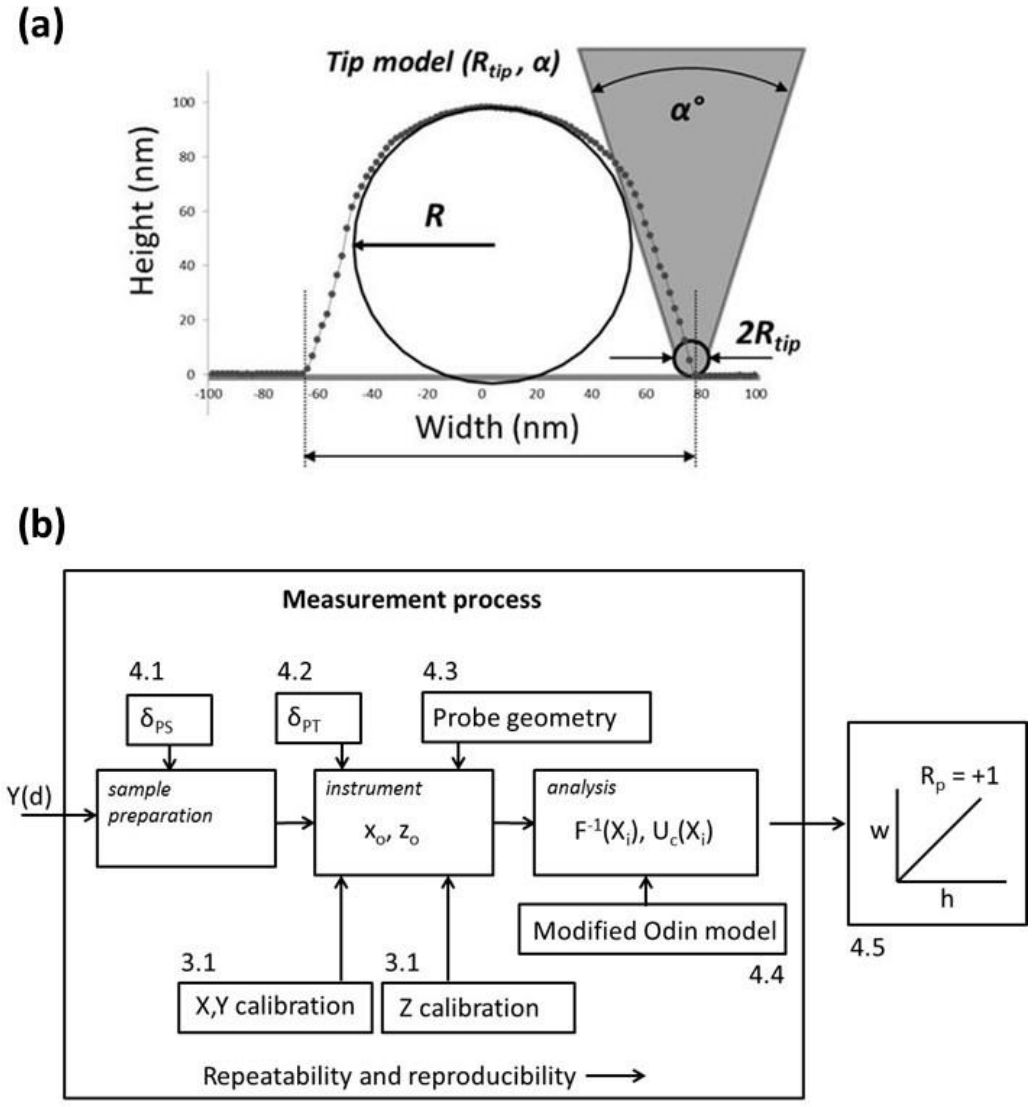

Figure 1. (a) Geometrical interaction between an AFM probe tip and a spherical particle. (b) Measurement process for correlated AFM height and width determination of an individual nanoparticle based on Ref. [9].

The measurand is therefore defined as the spherical diameter, $d = 2 \cdot R$, obtained from self-consistent fitting of an individual AFM image cross section. Fitting experimental apparent height and width data in terms of (x_o, z_o) yields a single value for the corrected particle $d(h) = d(w)$, parameterized by (R_{tip}, α). It is evident that R_{tip}, and α must be known in order to solve for R and we implement tip characterization as an essential modification of the model below. We consider a further modification of the Odin model by introducing corrections for δ_{PS} and δ_{PT} along the lines of the work of Garnaes as well.

The measurement process is summarized in Fig. 1b: Y(d) refers to the measurand, the diameter of a spherical particle, d. The instrument (transducer) output X_1 is given as a function of (x_o, z_o) and influence quantities, X_i, arising from sample interaction, instrument calibration, and model assumptions. Estimates of the measurand, $F^{-1}(X_i)$, and combined uncertainty, $U_c(X_i)$, are obtained self-consistently. Elements of the model are labeled with the section numbers in which they are discussed: Calibration is described in Sec. 3.1. The interaction model of Odin now includes explicit contributions for $X_i = \delta_{PS}, \delta_{PT}$, and the AFM probe-tip parameters, R_{tip} and α and these quantities are evaluated in Sec. 4.1, Sec. 4.2, and Sec. 4.3, respectively. These parameters are combined into the model as discussed in Sec. 4.4. The correlation coefficient, R_p, between d (h) and d (w) is shown to be a useful metric for evaluating parameter values in Sec. 4.5.

Sommer & Siebert emphasized the importance of recognizing whether or not a measurement process may adequately be described as under steady state control [9]. Nanoscale fracture and wear of an AFM probe tip is inevitable during imaging. The stability of the electro-mechanical control loop of the instrument is also subject to subtle physical and chemical changes in the operating environment, instrument, and sample. We follow their suggestions in the present work by classifying influence parameters as either static or dynamic on the time scale of the measurement.

3. Calibration

3.1 AFM calibration

A Veeco MultiMode AFM with Nanoscope IV controller, series J scanner, and v.6 software was used for imaging and particle size analysis. Imaging was performed in TappingMode using Bruker OTESPA (k = 42 N/m, f_o = 300 kHz) silicon probes. The microscope was shielded from air currents in a hood and the room was maintained under constant temperature and relative humidity, (23 $\pm$ 0.5) ºC and (28 $\pm$ 8) % RH, respectively. Control settings for AFM imaging were drive voltage = 2 V; an initial set point voltage is established at 85 % or approximately 1.7 V; Sensitivity of the OTESPA cantilever is typically 90 nm/V. [The amplitude (in nanometers) is related to the set point voltage (in volts) by a sensitivity factor (nm/V) which is obtained by calibration.] Free-oscillation amplitude is then approximately 180 nm and imaging amplitude is 150 nm. Optimized tapping-mode AFM operating conditions are established by monitoring topography, phase angle, and amplitude channels during imaging. For a specific AFM probe tip, the set point voltage value may need to be adjusted slightly to account for properties of the resonant cantilever and probe geometry. AFM measurement data presented here were obtained in the side-to-side scan direction and a strategy of employing a minimum number of tip-sample approaches during the acquisition of the image dataset was adopted to reduce tip fracture.

AFM scanner calibration of the lateral fast-scan, or X axis direction, was performed using a 70 nm pitch standard grating maintained at NIST [10, 11]. The calibrated value is stated as (70.055 $\pm$ 0.027) nm. The calibration was further verified with a line average measurement of nominally 1 µm PSL spheres, NIST standard reference material (SRM 1690) certified to be (895 $\pm$ 8) nm in diameter. Calibration of the height, or Z axis, was performed using a set of NANO2 step height reference standards over the range of

7 nm to 700 nm [11]. The resulting X and Z values were fit to a polynomial correction, linear in the case of X and quadratic in the case of the Z. Calibration correction values were checked periodically during the measurement cycle and were found to vary by < 1 %.

3.2 Determination of AFM probe shape

Figure 2 presents an AFM image of the Si/SiO_2 multilayer tip characterizer used in this study [10, 11]. Briefly, the structure is formed by magnetron sputtering of the alternating multilayers, wafer bonding to form a support, cross-sectioning and polishing the specimen, and finally selective etching. This process produces trenches with well-defined width and depth. The depth of the etched trenches is approximately 80 nm, feature width varies from 15 nm to 60 nm, and the between-feature spacing varies from 10 nm to 70 nm. A cross section through the image, superimposed with the nominal values for this characterizer structure, is shown in Fig. 2b. The AFM probe is able to access only some portions of the narrow trench; this information will be used to create a 2D reconstruction of the AFM probe shank. An estimate of the tip radius is obtained from information along the top of the knife-edge feature.

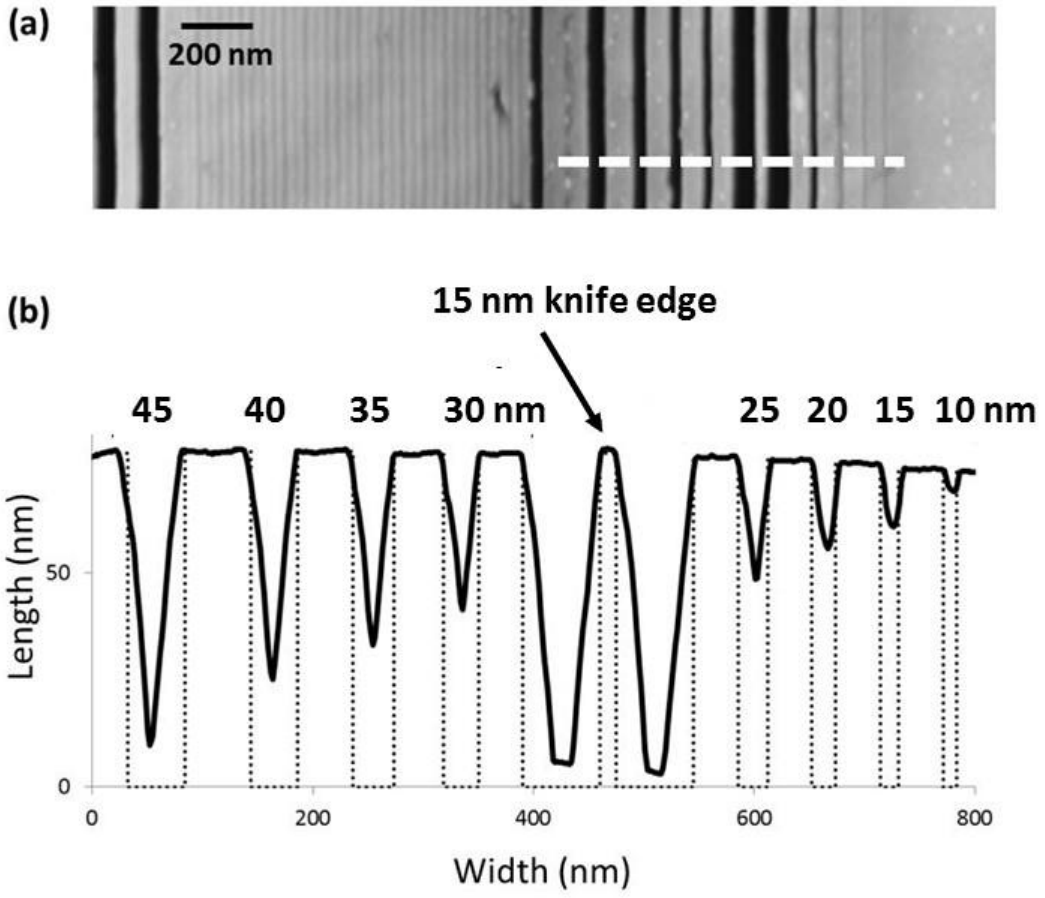

Figure 2. Schematic of the Si/SiO_2 multilayer tip characterizer. (a) AFM image and (b) cross section.

The characterizer provides two approaches to tip estimation: In the first, cross-sectional data from trench structures of known dimension allow determination of tip width based on the distance from the tip apex. The width of a specific trench, W, and length that the tip penetrates into it, L, represent contact points between the tip and characterizer encoded by (L, W) in the cross sectional AFM data. In the second, the knife-edge indicated in Fig. 2b may be used. After subtracting the line width of the knife edge, cross-sectional segments are inverted in both x and y directions. This allows for a consistency check of the final estimate of the 2D tip profile.

3.3 SEM calibration

An FEI scanning electron microscope (SEM) was used to image rafts and individual particles of PSL reference particles. A working distance of 3.7 mm, accelerating voltage of 5 keV, and beam current of 0.34 nA were used to obtain all images. The magnification of the instrument was calibrated using a 100 nm VLSI grating sample traceable to NIST. The calibrated value is stated as (99.936 $\pm$ 0.062) nm. The pixels-per-particle count was maintained between 40 and 48 in order that SEM image resolution would match that of corresponding AFM images. Threshold intensity was determined using the ImageJ maximum entropy function. The effect of beam exposure on particle size was determined to be 0.5 % or less for 100 nm PSL particles. All imaging was carried out on uncoated samples.

4. Measurement

NIST PSL SRMs 1964, 1963a, and 1691, with nominal diameters of (60, 100, and 300) nm were obtained from inventory. JSR PSL reference materials with nominal diameters of (30, 50, 70, and 100) nm, were obtained from JSR Life Sciences (Tokyo). PSL nanoparticles were attached to a poly-L-lysine coated mica substrate (Pella) or conductive single-crystal silicon chip for imaging. The sample was prepared by incubating a freshly cleaved mica or KOH-etched silicon substrate with 0.01 % poly-L-lysine (Sigma) for 10 minutes. The substrate was then blown dry with high-purity compressed air. A 10 µL drop of diluted nanoparticle solution was incubated on the substrate for 5 minutes, rinsed with DI water, and any remaining solvent removed by gently blowing with nitrogen gas.

AFM images of individual particles were analyzed using routines provided with the Veeco v.5 imaging software. A first-order image flattening routine was applied to obtain a global background suitable for obtaining particle height measurements. Particles in each image were identified by visual inspection and excluded before the background was calculated. To collect a statistically meaningful estimate of the particle size distribution, roughly $300 < N_p < 500$ nanoparticles were measured for each size. To obtain sufficiently flat background and enough pixels/particle, typically this requires 30 images containing 10 particles each to be analyzed. SEM images of individual particles were analyzed using ImageJ [15] by first applying a minimum threshold to eliminate background noise to each image and collecting a distribution of area-equivalent diameters for at least 500 particles of each particle size in accordance with ISO 13322-1 [16].

Representative images of the four JSR PSL reference materials are presented in Fig. 3. There are inherent advantages and disadvantages to raft and individual particle measurement approaches in terms of sample preparation, information content, and measurement uncertainty. Either method may be used for raft or individual particle analysis, although the measurands will differ.

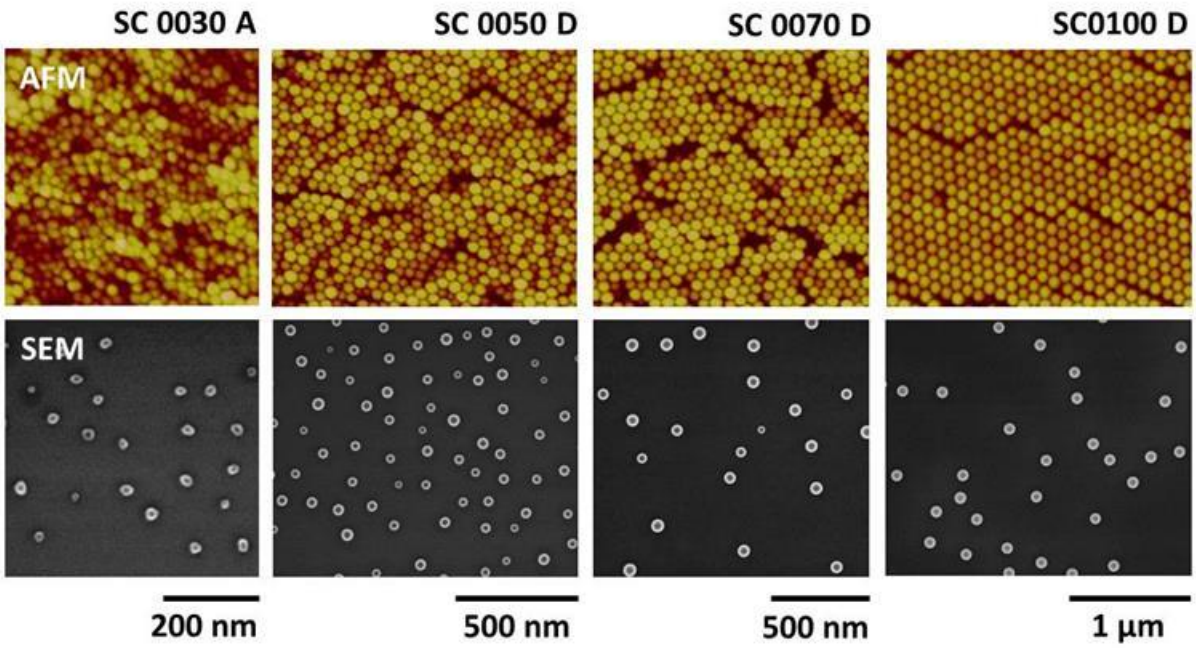

Figure 3. Images of nominally (30, 50, 70, and 100) nm diameter JSR PSL reference materials used in this study. AFM images (top) and SEM images (bottom) correspond to raft and isolated particles, respectively. A common scale bar appears below each column.

4.1 Particle-substrate deformation

PSL reference materials in solution are typically highly negatively charged colloidal systems, typically –70 mV < ζ < - 40 mV, depending on the solution environment. Attachment of PSL spheres onto a freshly cleaved mica substrate, for which ζ = - 80 mV, or a poly-L-lysine (PLL) coated substrate, for which ζ = + 80 mV, involves considerable rearrangement of interfacial charge. The compressibility of the particle assists the equilibrium electrostatic balance by allowing an increase in the contact area between the particle and substrate.

We are concerned that an elastic deformation model which neglects such interactions may not provide a reasonable quantitative estimate for the contact area that would develop in this case. In particular, it may substantially underestimate the deformation that a PSL particle experiences during sample preparation. The elastic deformation model was adopted by Garnaes following work of Grobelny et al. [17] in order to obtain an estimated uncertainty for δ_{PS}. Here we will approach the problem in terms of the more general Maugis-Pollock (MP) model which interpolates between the limiting cases of elastic and plastic models [18]. A theoretical discussion of this topic for AFM applications has been presented by Butt et al. [19]. We will reference our measurement results to recent experimental work by Wang et al. [20] which clearly reveals that deformation of PSL dimers are fully plastically deformed.

To establish a reference point for our particle-substrate deformation measurements, we consider the general MP approach to contact mechanics as outlined by Butt and somewhat modify the SEM technique of Wang. In this case we obtain SEM images of uncoated PSL dimers for nominally (60, 100, and 300) nm diameter NIST PSLs (SRMs 1964, 1963a, and 1691, respectively), shown in Fig. 4a. Dimers occur naturally in these solutions due to aging and can be located simply by surveying the sample.

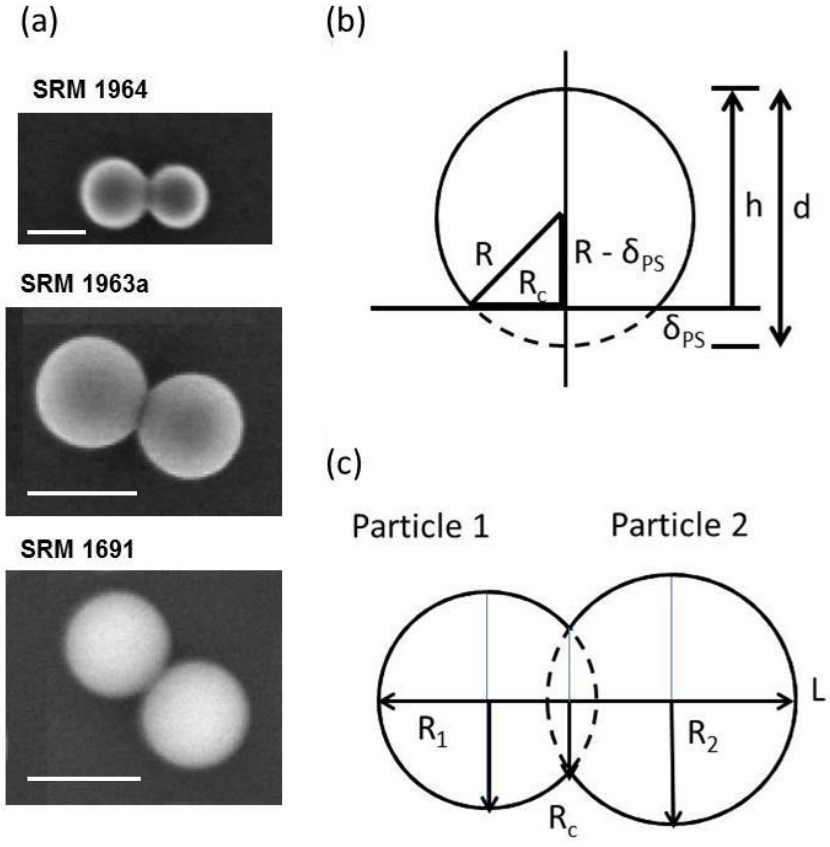

Figure 4. (a) SEM images of PSL dimers found in (60, 100, and 300) nm diameter NIST SRM sample solutions. Scale bars: (50, 100, 300) nm, respectively. (b) Geometrical relationship to extract deformation and contact radius, R_c, from AFM topography. (c) Geometrical relationship used to obtain R_c from SEM dimer images.

To avoid well-known difficulties associated with determining the contact radius (or contact area) from electron microscopy images, we extract contact radius and deformation from SEM dimer images using the geometrical relationships presented in Fig. 4b and 4c. For each SEM dimer image, we obtain undistorted particle radii, R_1, R_2, measured perpendicular to the dimer axis and the length measured along the dimer axis, L, as shown in Fig. 4b. This approach avoids direct measurement at or near the contact region where SEM image intensity is significantly attenuated. All distances are then defined between locations on the dimer with equal secondary-electron intensity. The contact radius, R_c, can be obtained from R_1, R_2, and L by simple trigonometry. Extraction of a contact radius and particle-substrate deformation from AFM height measurements follows in a similar fashion, Fig. 4c, given that particle-tip deformation, δ_{PT}, may be neglected.

Particle-substrate deformation from combined SEM and AFM height measurements, δ_{PS}, vs. R_c is plotted in Fig. 5 for NIST PSLs (filled circles). Each data point consists of an average of several individual particle measurements, $N_p > 15$. Averaged SEM dimer measurements, i.e., particle-particle deformation, δ_{PP}, vs. the reduced radius are also plotted (open circles). Elastic and plastic limits according to the MP model are shown in the figure as well. These limits are found in Fig. 4 of Garnaes and Fig. 3 of Wang; theoretical background can be found in Section 4 of Butt.

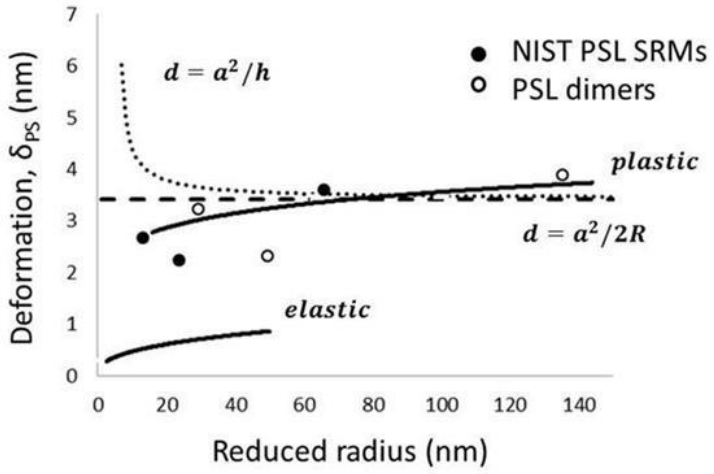

Figure 5. Average deformation of NIST PSL SRMs as a function of reduced radius. Theoretical behavior for the elastic and plastic limits is indicated by a solid curve. The dotted line represents an approximation for the plastic result appropriate for large reduced radius; the limiting MP result is indicated by the dashed horizontal line.

Figure 5 demonstrates unambiguously that PSL attachment during sample preparation can be described in the limit of plastic deformation. Deformation is defined within the MP model as $(2\ w_A/3Y)^{1/2} = R_c^2/R_{red}$, where w_A is the work of adhesion, Y is the yield point, R_c is the contact radius and R_{red} is the reduced radius. The limiting value of 3.4 nm appears as the dashed horizontal line in the figure. This limit is consistent with the behavior of particle-tip deformation past the yield point. Taken together with wet and dry attachment comparisons mentioned later, we conclude that the amount of deformation is determined by PSL material properties and not the work of adhesion. Therefore, alternative nanoparticle surface attachment methods should lead to comparable particle-substrate deformation. Only the 100 nm NIST SRM 1963a shows a somewhat lower value than the plastic model prediction for both AFM height and SEM dimer results.

4.2 Particle-tip interaction

In tapping-mode AFM, variation of the set point changes the oscillation amplitude of the integrated tip and cantilever. Fig. 6a illustrates that AFM operation is then largely determined by the set point voltage which (indirectly) controls the applied imaging force. Deformation is just the measured difference between apparent particle heights as the set point is changed. The set point voltage also determines how faithfully the AFM feedback loop probe tracks topographical features; consequently, it may be affected by the stability of the electromechanical system and unintentional modification of the AFM probe tip.

To establish an operational definition for a *zero-deformation condition*, $\delta_{PT} = 0$, there are different ways to proceed: We might use the fact that the AFM can sense a minimally detectible interaction between the particle and tip, such as with a force-distance curve, and then determine whether or not a measurable deformation of the particle has occurred at that point. On the other hand, such a small force may be insufficient for the feedback loop to maintain tracking of the particle shape during imaging, so we might want to consider the minimal observable deformation under imaging conditions. It is not immediately clear how close or far away these conditions may be.

Operationally, we seek an optimal value of the set point which is the maximum overlap of these two criteria: the minimally detectible interaction and minimal observable deformation under imaging conditions. This is indicated by the vertical line in Fig. 6a. In the force-distance mode (otherwise referred to as force-volume imaging in this work), the AFM probe approaches a particle from a position of zero force until a preset interaction force, the trigger point, is detected. At that point, the probe is retracted and the apparent height at which the interaction was detected is recorded. Decreasing the trigger point from the free-oscillation voltage to the imaging set point voltage provides an estimate of the first criterion. Imaging at the highest set point for which good real-time tracking can be maintained (arguably operator defined) and its *observed* deformation, if any, provide an estimate of the second.

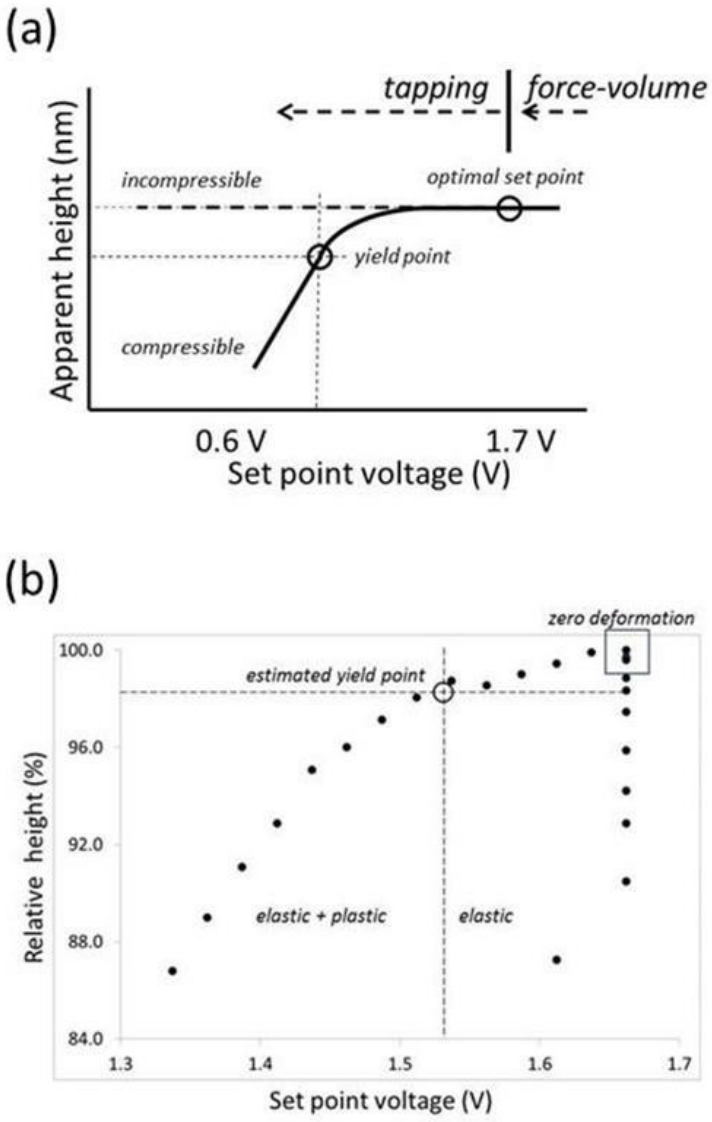

Figure 6. (a) Measurement principle used to investigate particle-tip deformation, δ_{PT}, of compressible particles. (b) Experimental height vs. set point voltage data. Each data point is an average of the same15 PSL particles as the set point voltage is reduced by 0.025 V/step.

But what happens if the set point drifts away from, or was not properly set to, this optimal value? The principles of tapping-mode AFM operation and contact mechanics lead us to expect that distinctly different compressibility behavior will emerge as the set point is decreased (or the force is increased). The transition from elastic to plastic behavior, the *yield point*, is a familiar concept; it is indicated by a circle in Fig. 6a. However, the possibility that the system wanders into the regime of elastic-plastic interactions in which subsurface material damage may occur must be considered. Regimes of PSL compressibility that may be encountered during AFM imaging, elastic, elastic-plastic, and pure plastic deformations, must be identified precisely.

We can remove the size dependence by normalizing and averaging individual PSL height data for a number of particles from a single image. Data for 15 particles from the same image stack were averaged and the aggregate behavior is presented in Fig. 6b. The box appearing on the upper right side of the graph indicates the narrow window for optimal AFM imaging of deformable particles, approximately 0.05 V. The region of elastic deformation extends from 1.54 V < A < 1.67 V in the figure. The region of plastic deformation for which the height never recovers is given by A < 1.54 V.

Additional discussion of particle-tip interaction forces is taken up in the Appendix.

4.3 Probe geometry

The fabrication process used to manufacture silicon AFM probes is based on selective etching of single-crystal silicon. In the case of OTESPA probes, this process yields an asymmetric tip geometry with a nominal 35° tip angle, and a 10° tip holder tilt. The term "front-to-back" is used in this article to identify the alignment of the long cantilever axis to the fast-scan, or microscope X axis, direction. Conversely, the term "side-to-side" refers to alignment of the narrow cantilever axis to the fast-scan, or microscope X axis, direction. The final 500 nm or so of the shank do not follow the etching geometry since oxide sharpening of the tip apex significantly narrows the width of the tip angle and yields a nonzero orientation with respect to the surface plane. In contrast the final probe geometry in the side-to-side direction is symmetric. In this case, the nominal tip angle of $\alpha = 35°$, is reduced to $12^o \leq \alpha \leq 13°$ and the angular orientation of the probe axis with respect to the surface plane is zero degrees.

The occurrence of tip wear during imaging is inevitable. On the one hand, catastrophic damage is easy to spot; more gradual processes, on the other hand, introduce uncertainty in particle width measurements which are more subtle. So, determination of the sensitivity of AFM particle size measurements to both fracture and continuous wearing of contact surfaces of the probe tip and shank must be considered. Here again, it is important to recognize that tip wear depends upon the scan direction of the tip: Tip wear is symmetric in the side-to-side direction and its angles and orientation remain unchanged even after extensive tip wear has occurred. By contrast, the wear pattern is highly asymmetric in the front-to-back direction and orientation of the tip with respect to the surface plane then changes rapidly. Inherent asymmetry of the front-to-back angle produces a rapid increase of the width of the tip as a result of even moderate wear.

Wear testing of two different probes is presented for side-to-side imaging and back-to-front imaging, Fig. 7a and 7b, respectively, for accelerated wear conditions, i.e., set points were varied from 1.2 V to 1.5 V, compared to typical set points for OTESPA probes, 1.6 V to 1.7 V. In the case of front-to-back imaging, the front tip edge shows very little wear, whereas the back side suffers almost all the damage resulting from fracture and wear. Silicon probe tips are most likely to fracture during the engagement of feedback control and this operation effectively determines the initial tip apex [21]. For side-to-side imaging the fracture and wear patterns tend to be more symmetrical. Alignment of a reconstructed tip shape to an SEM image indicates that actual tips retain the characteristic probe geometry rather well despite undergoing some degree of arbitrary fracture and wear. This greatly simplifies the entire problem

of tip characterization because it allows us to adopt the tip model shown in Fig. 1a. Furthermore, the conical tip function, parametrized by (R_{tip} α), is largely independent of wear, i.e., the probe-tip angle, α, remains essentially constant.

Measurement sensitivity then depends mainly on how R_{tip} is affected by typical fracture and wear patterns. Monitoring changes in the tip radius with the characterizer provides a way to estimate the rate of change of the effective radius with wear. No change due to wear was observed for set point values between 1.6 V and 1.7 V when using the characterizer. Wear behavior of the tip in the front-to-back scan direction is such that the overall shape of the tip deviates increasingly from the conical tip model as it wears and this has a large effect on the tip radius. Conversely, the average tip angle persists in the side-to-side scan direction. Because of the symmetrical wear and retention of steep angles, tip wear can be monitored by simply correcting for the tip radius when side-to-side imaging is employed.

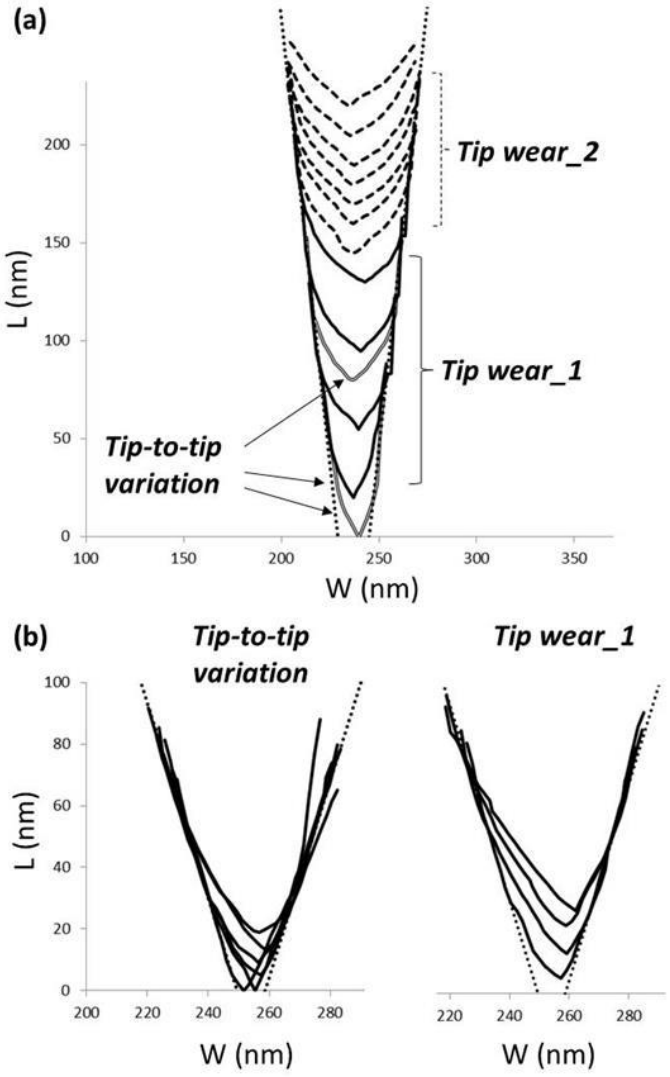

Figure 7. Reconstructed AFM probe tip profiles in the (a) side-to-side and (b) front-to-back tip directions. Profiles for a previously unused and a severely worn tip (Tip_1 and Tip_2) are shown aligned to a common orientation of the probe axis (dotted lines).

4.4 Cross-sectional analysis

Figure 8 illustrates how it is possible to obtain a self-consistent estimate of the measurand, Y(d). The output function of the measurement is the AFM cross sectional data (x_o, z_o) for an individual PSL particle fit according to the Odin model (dashed line). The modeling result is given by the solid line. This figure provides a comparison of measurement data and model fits for 50 nm, 70 nm, and 100 nm diameter JSR PSL particles. Good correspondence between the AFM cross sectional data and the modified Odin model can be achieved over a wide range of particle sizes. For this example, a constant value of δ_{PS} = 3.4 nm from Fig. 5 was found to be a sufficiently precise value for these PSL samples. A fixed tip angle of α = 12.5° is a good assumption for imaging in the side-to-side scan direction. Nominal values of R_{tip} = 7 nm and δ_{PT} = 0 nm are assumed initially. It is important to recognize that more information is available from AFM cross-sectional data which allows an improved estimate of R_{tip}. Two-dimensional information is shown in the areas shaded in gray in the figure. Here the cross section encodes the particle-tip contact interaction without induced δ_{PT} deformation because the major component of the total force of the tip on the particle in these regions is non-normal and, as a consequence, δ_{PT} is insignificant. This is certainly not the case as the AFM probe scans near the particle apex and some evidence of particle-tip deformation is evident in the cross-sectional data for all three particles.

With a good estimate for R_{tip}, a nonzero value of δ_{PT} near the particle apex region may be obtained by an iterative fitting process. Of course, if there were no prior knowledge of δ_{PS}, there would be no unique solution, Y (d) = 2·R, where R is the particle radius. For example, equally acceptable fits of the AFM measurement data can be obtained for the set of parameters {R: δ_{PS}, δ_{PT}, R_{tip}, α} and a value of R from 48.1 nm to 51.5 nm can be obtained for different combinations of δ_{PS}, δ_{PT}, R_{tip} and α. Evidently, an understanding of the deformation and tip submodels is needed to avoid errors of 7 % or more. In particular, a value of $\delta_{PS} \leq 1$ nm for *elastic* particle-substrate deformation would result in an error of several percent in the determination of the particle radius.

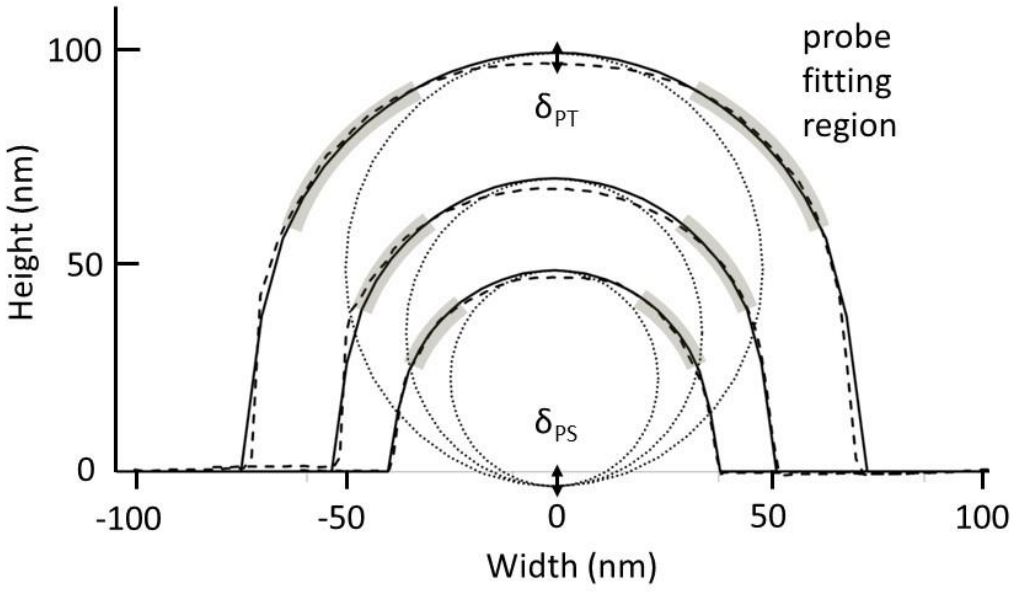

Figure 8. Cross-sectional fitting using the modified Odin model. (a) AFM measurement data (dashed line) is plotted along with a fit to the model (solid line) for three particle sizes. A constant value of δ_{PS} = 3.4 nm provides a satisfactory fit for all 3 particles.

4.5. Dynamic error correction

Analysis of particle size measurement data in metrology is based on statistical principles. For this reason, it is not practical, or necessary, to fit cross sections for each of the 1 700 JSR particles measurements described below. So, let's change focus from an individual particle measurement as shown in the previous figure to a more distributional point of view. A complete fitting of (x_o, z_o) data is not necessary because a 2-parameter representation of the full AFM height, $z_o = z_{max}$, and width, $x_o = 2 \cdot \Delta L_{1/2}$, in the Odin model can be calculated directly if δ_{PS}, δ_{PT}, R_{tip}, and α are estimated reasonably well. These parameters are known or can be calculated from the model using a representative sampling of individual particles from a sequence of image files.

An example of this error correction procedure is illustrated for the set of data files listed in Table 1 and plotted in Fig. 9. Figure 9a, the upper curve, consists of initial height and width values corrected for Z and X calibration errors only. The swarm of data points is clearly nonlinear, so calculating average size does not properly account for dynamically changing influence quantities. Table 1 contains a color-coded listing of six AFM OTESPA probes used to collect height and width data for the four JSR particles along with the associated number of image files. A given AFM tip may acquire imaging data for more than one particle-size sample. Particles within each image file are recorded sequentially and for each subset of particles corresponding to a given AFM tip and image file, one particle is fit to the full model and updated values for δ_{PT} and R_{tip} are then applied to calculate a corrected set of height and width values for the remaining image file.

Table 1. Guide to the data appearing in Fig. 9.

Tip number (#)	Color code	JSR PSL particle size (nm)	Number of image files averaged (#)	Range of set point voltage (V)	Average tip radius R_{tip} (nm)	Average particle-tip deformation δ_{PT} (nm)
1	Red	30 50 50 100	4 3 3 2	1.687 1.687-1.637 1.662-1.612 1.662	11.0 11.0 11.0 13.0	0.0 4.9 2.4 1.1
2	Green	30 50	3 2	1.687 1.687	7.0 14.3	0.0 0.0
3	Blue	50 30 100	5 2 14	1.687-1.512 1.637 1.637-1.612	12.8 13.0 22.0	1.0 0.0 3.6
4	Gold	50 50	3 3	1.687-1.662 1.587-1.562	14.2 15.7	0.0 0.0
5	Magenta	70 70	4 4	1.637-1.587 1.612-1.462	14.5 14.8	2.1 2.4
6	Black	70	3	1.687-1.637	12.5	0.0

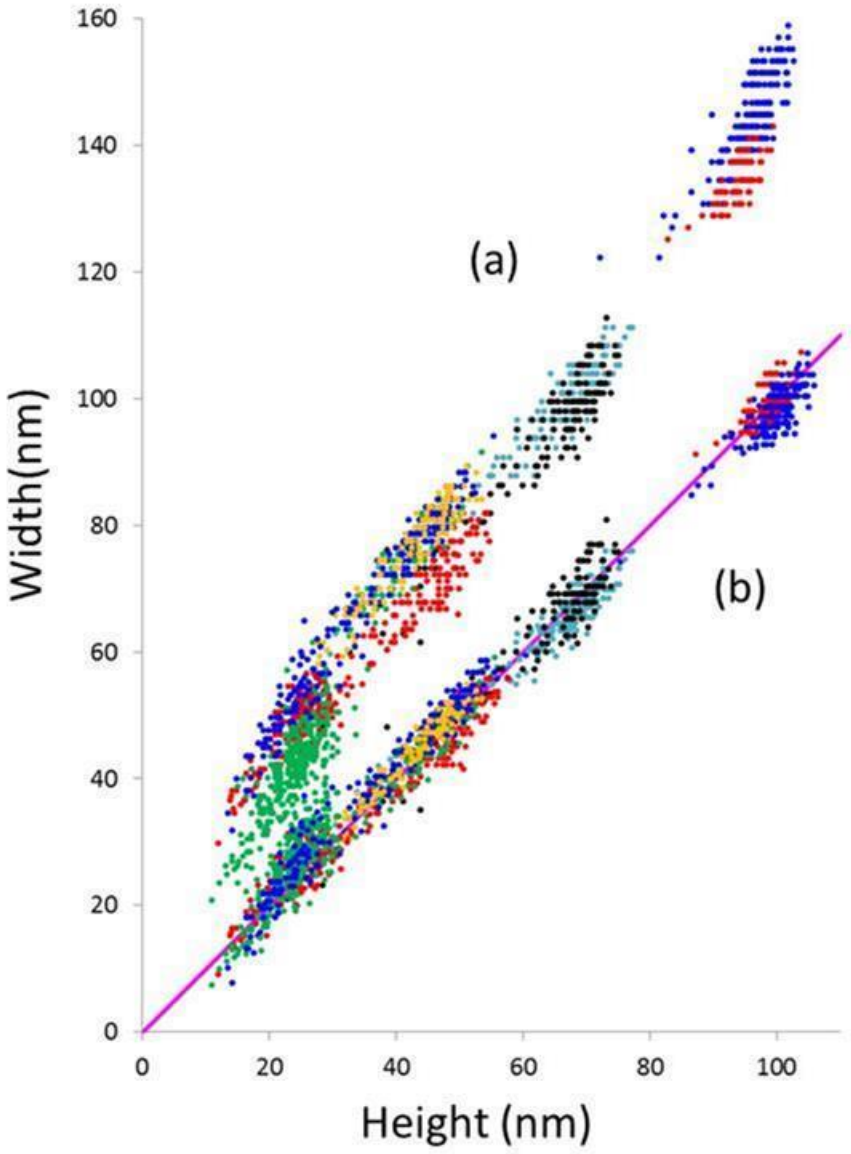

Figure 9. Correlated AFM height and width data for the four JSR particle sizes and six different AFM probes listed in Table 1. (a) Apparent height and width corrected for Z and X calibration only. (b) Same data set after correction for δ_{PS}, δ_{PT}, and R_{tip}.

Figure 9b represents the swarm of data points after δ_{PS}, δ_{PT} and R_{tip} correction. It reflects an alignment of the data along the 1:1 reference line, i.e., a (Pearson's) correlation coefficient of $R_p = +1$ relation between corrected height and width values. This relation holds independent of particle size and other factors such as AFM tip condition and potential set point drift. The measurement approach proposed here is based on statistically relevant datasets of correlated AFM height and width measurements. Given the inevitability of tip wear, we seek to minimize its influence in the course of collecting $N_p > 500$ individual measurements and by correcting for tip wear during the analysis stage. For a given set of image files, a monotonic increase in R_{tip} is observed due to tip wear. On the other hand, the set point voltage which largely determines δ_{PT} is subject to operator intervention and electro-mechanical drift of the instrument. The magnitude of particle-tip deformation can be seen to increase or decrease at times as a result of these

adjustments. Also note that the height and width values plotted in Fig. 9 appear discrete. This reflects the limited number of pixels used to acquire the image. In particular, this effect is more pronounced for larger particle sizes. It underscores the need to optimize a number of quality control factors during sample preparation and data acquisition such as the average particle density per image and the number of images needed for a distributional analysis. These factors influence the range of scan size, pixel size, and number of pixels that overlay a single particle and evidently set a lower limit on the measurement error that may be claimed.

It is worth emphasizing once again that the significantly better agreement between corrected height and width values for the 1700 particles presented in Fig. 9 could be achieved with relatively little additional cost: Only one cross section for a single particle contained within each of the 55 image files listed in Table 1 was analyzed according to Fig. 8. The set of updated δ_{PS}, δ_{PT} and R_{tip} parameters were then used with Eqns. (1) to (3) to analyze the remaining number of particles for each image file. This extra effort seems worthwhile to obtain such a dramatic improvement in measurement quality.

4.6 Validation of the measurement model

Particle height data from Fig. 9 is grouped according to sample size in Table 2. The average height corresponding to data shown in Fig. 9a, which includes a calibration correction only, is seen to be significantly smaller than the average height corresponding to data shown in Fig. 9b, which also includes the deformation corrections, δ_{PS} and δ_{PT}, determined from the dynamic error correction scheme described above. The height difference represents a substantial reporting error if not adequately taken into account.

Figure 5 indicates that δ_{PS} is nearly constant across the nanometer-scale particle size range of interest here. Uncertainty related to the dynamic influence of δ_{PT}, however, is more difficult to specify although it may also make a large contribution to the overall deformation. For example, a particle height difference of 4 nm will occur for a 60 nm particle if a set point voltage of 1.50 V is used rather than the optimal value near 1.65 V, a difference of almost 9 % resulting solely from δ_{PT}.

We believe such a contribution may account for the discrepancy between AFM height measurements reported by Garnaes and those obtained in this work for the NIST SRM 1963a. Mean *uncorrected* AFM height and width (h, w) estimates based on our measurement model are 96.5 nm and 98.8 nm, respectively. Values reported by Garnaes are 92.3 nm and 98.9 nm. Width estimates are identical but height estimates are considerably different. The difference, $\Delta = w - h$, is 2.3 nm for our values and 6.6 nm for his. This latter difference is too large to be accounted for by the fixed uncertainty estimates given by Garnaes, $\delta_{PS} = 2$ nm and $\delta_{PT} = 0.5$ nm. (This inconsistency was recognized, but not accounted for, in the article.)

Table 2. Average AFM height for the JSR PSL particle data shown in Fig. 9. N_p is the number of particles of each size analyzed in Table 1.

JSR	Number of particles, N_p	Fig. 9a Height and standard deviation (nm)	Fig. 9b Height and standard deviation (nm)	Difference Δ(h) (nm)
30	545	(20.4 ±4.0)	(23.8±4.0)	3.4
50	517	(39.3±7.1)	(44.0±7.2)	4.7
70	328	(60.1±9.4)	(64.8±9.2)	4.7
100	318	(93.8±3.8)	(99.2±4.0)	5.4

To investigate the degree to which the *corrected* AFM height and width data represent a self-consistent solution, i.e., $\Delta = w - h = 0$, we plot a subset of the 50 nm JSR data from Fig. 9 in Fig. 10. The height and width data are also shown as separate size distributions in blue and red, respectively. A glance at Table 1 indicates that these data for $N_p = 517$ particles were collected from19 image files using 4 different AFM probe tips from measurements made on 4 separate days.

The peaks of these distributions coincide at a diameter of (47.0 $\pm$ 4.0) nm, which is larger than the average diameter value of (44.0 $\pm$ 7.2) nm given in Table 2. This is because the particle size distribution for the JSR 50 nm is somewhat negatively skewed. However, this difference lies within one standard deviation of the average value. An (asymmetric Gaussian) fitting function from SEM analysis of the JSR 50 nm particles, where $N_p = 1\,596$ particles, is represented by a solid black curve superimposed on the AFM distributions. The peak value of the SEM distribution occurs at 46.5 $\pm$ 3.8 nm, equivalent to the AFM peak. This close correspondence is significant because the SEM measurand, defined in terms of an area-equivalent diameter, is not required to be the same as that from an AFM height or width cross-sectional measurement. That all three values coincide is strong evidence that the abstract spherical model is self-consistent within the AFM measurement model and valid across imaging methods as well.

Similar results are obtained for the other JSR and NIST PSL particles although lower particle counts, N_p, for both AFM and SEM data sets make the comparison slightly less compelling.

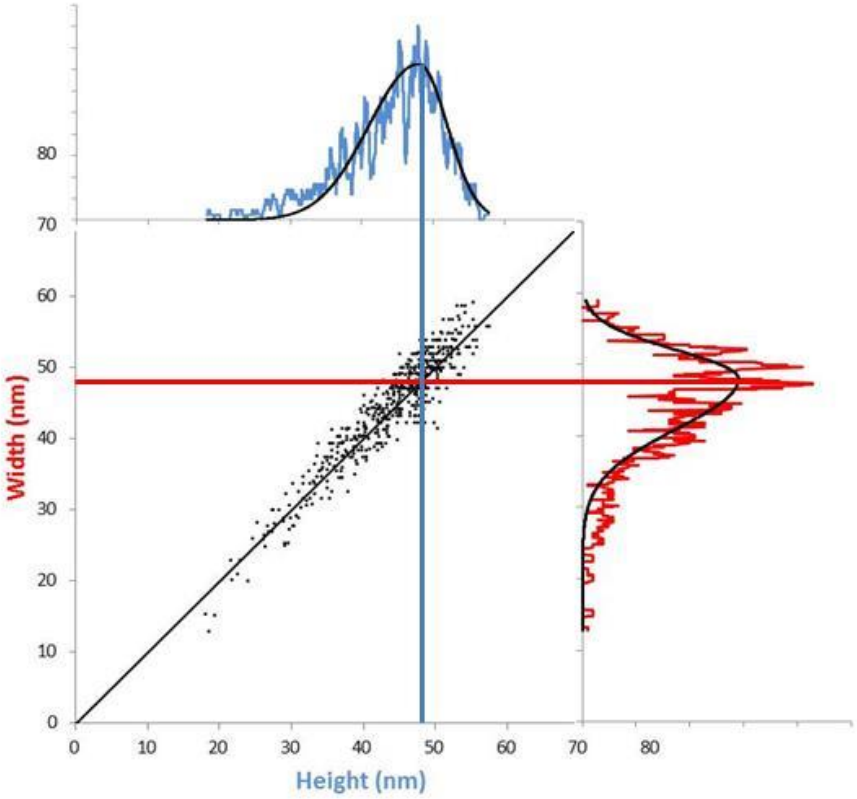

Figure 10. Correlated AFM height and width for the 50 nm diameter JSR particles (filled circles). This is a subset of the data presented in Fig. 9b. Size distributions for the height and width appear in blue and red, respectively.

5. Uncertainty analysis

Influence quantities considered to be significant for the measurement model are described briefly below. An example of estimated uncertainties for the 100 nm JSR particle is given in Table 3. Normal distributions are assumed for Type A and rectangular distributions are assumed for Type B quantities. Following the table, combined and expanded relative standard uncertainties, u_c and U_c, respectively, are given for the nominally 100 nm diameter particle with estimates derived from height and width corrections calculated separately. An asterisk indicates that the non-steady state parameter value must be determined as part of the error-correction scheme presented in Sec. 4.5.

Influence quantities for the height measurement:

Type B: Particle-substrate deformation

We adopt the Maugis-Pollock result for pure plastic deformation of a polystyrene sphere, 3.4 nm, as a systematic correction of the measured apparent height. There is some further uncertainty of this value for a specific particle sample because of size dependence and compositional variations. From the results shown in Fig. 5 and measurements of other PSL samples, we include an additional random component of $\pm$ 0.7 nm.

Type B: Particle-tip deformation

This quantity is sampled periodically and updated for each image file as part of the error-correction scheme. We can then assume image-to-image variation to be zero nanometers. Sampling of individual particles within a single image yields an estimate of about $\pm$ 0.5 nm about the current value.

Type B: Z calibration and hysteresis

NANO2 step heights are reported to have an expanded uncertainty of U_c = + 1.1 nm or less for the range of artifacts used in this study. Measurements of these artifacts before and after a day's worth of imaging indicated a change in calibration of no more than $\pm$ 0.6 nm. Repeated sequential measurements of the same artifact yielded a drift of $\pm$ 0.3 nm from image to image.

Type B: Background flatness

Measurement of the topographical roughness of substrates used in this work, freshly cleaved mica with a coating of 0.01% poly-L-lysine, indicates a peak-to-valley roughness of $\pm$ 0.5 nm or less for the range of scan sizes used in this work, 500 nm to 2 μm.

Type A: Instrument noise and measurement repeatability

Analysis of incompressible gold particles attached to poly-L-lysine coated mica substrates indicates the topographic repeatability of the faceting of individual gold particles is $\pm$ 0.3 nm. This reflects the capacity of the AFM to maintain stable feedback operation over multiple image scans. For PSL particles which are compressible, the repeatability increases to $\pm$ 0.7 nm. For the measurements reported here, we assume that the former represents an instrumental noise uncertainty while the latter is relevant for the sample type of interest here.

Influence quantities for the width measurement:

Type B: AFM probe radius, angle and wear rate

Nominal values provided by the manufacturer for the tip radius and probe angle of a fresh tip are 11 nm and 12.5°. Experience with these probes indicates that a typical tip radius varies by no more than $\pm$ 4 nm from the average and the angle by less than $\pm$ 0.5° from the average side-to-side orientation. Since the tip radius is sampled periodically and updated for each image file as part of the error-correction scheme, we assume image-to-image variation to be zero nanometers due to the measurement. A geometrical

argument suggests that the angle uncertainty contributes ± 0.4 % Accumulated tip wear over a single image scan is below 0.8 nm/image. This estimate refers specifically to imaging in the side-to-side scan direction and translating without mechanically retracting the probe tip.

Type B: X calibration and hysteresis

The ASM sample is reported to have an expanded uncertainty of U_c = ± 0.027 nm. Measurement of this artifact before and after a day's worth of imaging indicated a change in calibration of no more than ± 0.3 nm.

Type B; Validity of the tip model

The uniqueness of the probe geometry obtained by fitting the modified Odin model to test data indicates that the tip radius can be determined to within ± 3 % of the particle diameter. Note that the particle-tip and particle-substrate deformation were allowed to vary for this estimate.

Type B; Pixel resolution

An important criterion for good particle size measurements is the rule to select the image scan size so that a minimum of 40 pixels spans the average particle diameter. However, as the pixel size is decreased to accommodate small particle sizes, the probe tip radius remains essentially constant. This mismatch is therefore inversely proportional to particle diameter for particles less than 100 nm in diameter, on the order of 1 % for 30 nm particles.

Type A: Repeatability

Repeatability of the instrument in the fast-scan direction is estimated to be about ± 1.5 nm for image-to-image comparison of a well-characterized 2D grid sample. The grid has 2 µm and 3 µm periodic structures and this estimate is an average over the range of scan sizes used in this study.

Table 3. Influence quantities, *x*, and estimated uncertainties, u(*x*), for the measurement model. Entries are completed for the 100 nm JSR particle size for which the corrected average diameter estimates are d(h) = 99.2 nm and d(w) = 98.4 nm.

Height				**Width**			
Component	*x* (nm)	u(*x*) (nm)	%u(*x*)[a]	Component	*x* (nm)	u(*x*) (nm)	%u(*x*)[a]
δ_{PS}	-3.4	0.7	0.7	R_{tip} (11± 4) nm	0*	0 nm	0
δ_{PT}	0*	0.5	0.5	Tip wear rate (nm/image)	0 *	0.8 nm/ image	0.8
				α (12.5± 0.5)°	0		0.4
Z calibration	0	0.6	0.6	X calibration	0	0.03nm	0.03
Z hysteresis	0	0.3	0.3	X hysteresis	0	0.3 nm	0.3
Background flatness	0	0.5	0.5	Validity of the tip model	0		3
				Pixel resolution	0		$2800 \cdot d^{-2}$
Instrument noise	0	0.3	0.3				
Repeatability	0	0.7	0.7	Repeatability	0	1.5 nm	1.5

[a] $\%u(x) \equiv 100 \cdot u(x)/x$

Combined Relative Standard Uncertainty:

The combined relative standard uncertainty of the Type A components for particle diameter is:

$$\%u_{\mathrm{A}}(d) = \sqrt{\sum_{i=7}^{8} \%u^2(x_i)}$$

where $u(x_i)$ are normal-distribution standard uncertainties for components 7 and 8 listed in Table 3. As determined from the height calculation, $\%u_{\mathrm{A}}(d(h))$ = 0.76 % and $\%u_{\mathrm{A}}(d(w))$ = 1.5 % from the width calculation.

The combined relative standard uncertainty of the Type B components is:

$$\%u_{\mathrm{B}}(d) = \sqrt{\frac{1}{3}} \sqrt{\sum_{i=1}^{6} u^2(x_i)}$$

where $u(x_i)$ are uniformly distributed relative standard uncertainties for components 1 to 6 listed in Table 3. As determined from the height calculation, $\%u_{\mathrm{B}}(d(h))$ = 0.69 % and $\%u_{\mathrm{B}}(d(w))$ = 1.8 % from the width calculation.

The complete combined relative standard uncertainty of the diameter measurements is then:

$$\%u(d) = \sqrt{u_{\mathrm{A}}^2(d) + u_{\mathrm{B}}^2(d)}$$

As determined from the height calculation, $\%u(d(h))$= 1.0 % and $\%u(d(w))$= 2.4 % from the width calculation.

Assuming a coverage factor of k = 2, an expanded relative uncertainty for the droplet diameter estimated in this manner is

$$\%U_{k=2}(d) = 2 \cdot \%u(d)$$

As determined from the height calculation, $\%U_{k=2}(d(h))$ = 2.0% and $\%U_{k=2}(d(w))$ = 4.8% from the width calculation. Expanded uncertainties for all four JSR particle sizes are given in Table 4 of the next section.

6. Summary

The measurement method proposed here provides an effective strategy for analyzing a statistically significant number of PSL particle size measurements obtained from AFM imaging data. A self-consistent estimate for the average spherical diameter for particle size distributions of the four JSR PSL reference materials and their combined uncertainties are presented in Table 4. Height- and width-derived diameters agree to within 1 nm to 2 nm. Estimated uncertainty for the width-derived diameter is a factor of 2.2 greater than for the height-derived diameter.

This is consistent with the generally accepted view that AFM height measurements offer higher precision and accuracy than width measurements. However, the key point of this demonstration is to show how the modified Odin model and error correction scheme efficiently makes use of data already available within a standard image file. It is a promising method for characterization of future generation PSL reference materials.

Table 4. Average diameter and expanded uncertainty derived from adjusted height and width data for PSL particle data presented in Fig. 9b.

JSR	Number of particles, N_p	Adjusted height (nm)	$\%U_{k=2}(d(h))$	Adjusted width (nm)	$\%U_{k=2}(d(h))$	Δ(h-w) (nm)	$\frac{\%Uc(d(h))}{\%Uc(d(w))}$
30	545	23.8	8.6	25.6	19.0	-1.8	2.2
50	517	44.0	4.6	44.3	10.7	-0.2	2.3
70	328	64.8	3.2	64.2	7.4	1.3	2.3
100	318	99.2	2.10	98.4	4.8	1.0	2.3

Acknowledgments

The authors wish to thank Vipin Tondare and Gheorghe Stan (NIST) for providing constructive comments during manuscript preparation. PSL reference materials with nominal diameters of (30, 50, 70, and 100) nm were provided as a gift by JSR Life Sciences (Tokyo).

References

[1] K. Ehara and H. Sakurai, Metrology of airborne and liquid-borne nanoparticles: current status and future needs, Metrologia **47,** S83- S90 (2010). http://dx.doi.org/10.1088/0026-1394/47/2/S09

[2] T. P. J. Linsinger, G. Roebben, C. Solans, and R. Ramsch, Reference materials for measuring the size of nanoparticles, Trends in Anal. Chem. **30,** 18 - 27 (2011). http://dx.doi.org/10.1016/j.trac.2010.09.005

[3] F. Meli, et al., Traceable size determination of nanoparticles, a comparison among European metrology institutes, Meas. Sci. Technol. **23,** 125005 (2012). (15 pp) http://dx.doi.org/10.1088/0957-0233/23/12/125005

[4] A. Yacoot and L. Koenders, Recent developments in dimensional nanometrology using AFMs, Meas. Sci. Technol. **22,** 1222001 (20011). (12 pp) http://dx.doi.org/10.1088/0957-0233/22/12/122001

[5] J. Garnaes, Diameter measurements of polystyrene particles with atomic force microscopy, Meas. Sci. Technol. **22,** 094001 (2011). (8 pp) http://dx.doi.org/10.1088/0957-0233/22/9/094001

[6] I. Misumi, K. Takahata, K. Sugawara, S. Gonda, and K. Ehara, Extension of the gravity center method for diameter calibration of polystyrene standard particles with metrological AFM, Proc. SPIE vol.**8378,** 83780J (2012). http://dx.doi.org/0.1117/12.918528

[7] B.-C. He, W.-E. Fu, H.-C. Liou, S.-P. Pan, H.-M. Lin, and Y.-F. Chen, Deformation of polystyrene nanoparticles under different AFM tapping loads, Proc. SPIE vol. **8378,** 83780G (2012). http://dx.doi.org/10.1117/12.921451

[8] C. Odin, J. P. Aime, Z. El Kaakour, and T. Bouhacina, Tip finite-size effects on atomic force microscopy in the contact mode: simple geometric considerations for rapid estimation of apex radius and tip angle based on the study of polystyrene latex balls, Surf. Sci. **317,** 321 - 340 (1994). http://dx.doi.org/10.1016/0039-6028(94)90288-7

[9] K. D.Sommer and B. R. L. Siebert, Systematic approach to the modelling of measurements for uncertainty evaluation, Metrologia **43,** S200-S210 (2006). http://dx.doi.org/10.1088/0026-1394/43/4/S06

[10] R. Dixson et al., Multilaboratory comparison of traceable atomic force microscope measurements of a 70-nm grating pitch standard, J. Micro/Nanolith. MEMS MOEMS **10** 013015 (2011). http://dx.doi.org/10.1117/1.3549914

[11] L. Koenders, et al., Comparison on nanometrology: Nano2—step height, Metrologia **40,** 04001 (2003). (77 pp).

[12] H. Itoh, T. Fujimoto, and S. Ichimura, Tip characterizer for atomic force microscopy, Rev. Sci. Instrum. **77,** 103704 (2006). (4 pp) http://dx.doi.org/10.1063/1.2356855

[13] H. Takenaka, et al., AFM tip characterizer fabricated by Si/SiO2 multilayers, e-J. Surf. Sci. Nanotech, **9,** 293 - 296 (2011).

[14] R. Dixson, Report of Measurement, (2008) unpublished.

[15] NIH (www.imagej.nih.gov/ij).

[16] Particle size analysis – Image analysis methods Part 1: Static image analysis methods, ISO 13322-1:2004(E).

[17] J. Grobelny, N. Pradeep, and D.-I. Kim, Estimation of contact area of nanoparticles in chains using continuum elastic contact mechanics, J. Nanopart. Res. **10,** 163-169 (2008). http://dx.doi.org/10.1007/s11051-008-9434-8

[18] D. Maugis and H.M. P. Pollock, Surface forces, deformation and adherence at metal microcontacts, Acta Metallurgica **32**, 1323 (1984). http://dx.doi.org/10.1016/0001-6160(84)90078-6

[19] H.-J. Butt, B. Capella, and M. Kappl, Force measurements with the atomic force microscope: Technique, interpretation and applications, Surf. Sci. Rep. **59,** 1-152 (2005). http://dx.doi.org/10.1016/j.surfrep.2005.08.003

[20] X.-D. Wang, B. Chen, H.-F. Wang, and Z.-S. Wang, Adhesion between submicrometer polystyrene spheres, Powder Technology **214,** 447-450 (2011). http://dx.doi.org/10.1016/j.powtec.2011.08.047

[21] K.-H. Chung, Y.-H. Lee, and D.-E. Kim, Characteristics of fracture during the approach and wear mechanism of a silicon AFM tip, Ultramicroscopy **102,** 161 - 171 (2005). http://dx.doi.org/10.1016/j.ultramic.2004.09.009

[22] J. A. Forrest, K. Dalnoki-Veress, J. R. Stevens, J. R. and Dutcher, Effect of free surfaces on the glass transition temperature of thin polymer films, Phys. Rev. Lett. **77,** 2002-2005 (1996). http://dx.doi.org/10.1103/PhysRevLett.77.4108

[23] H. Zhang, Y. Honda, and S. Takeoka, Tapping-mode AFM study of tip-induced polymer deformation under geometrical confinement, Langmuir **29,** 1333-1339 (2013). http://dx.doi.org/10.1021/la304280h

[24] J. Tamayo and R. Garcia, Deformation, contact time, and phase contrast in tapping mode scanning force microscopy, Langmuir **12,** 4430-4435 (1996). http://dx.doi.org/10.1021/la960189l

[25] R. L. Jackson, and I. Green, A finite element study of elasto-plastic hemispherical contact against a rigid flat, ASME J. Tribol. **127,** 343-354 (2005). http://dx.doi.org/10.1115/1.1866166

[26] E. J. Abbot and F. A. Firestone, Specifying surface quality – a method based on accurate measurement and comparison, Mech. Eng. (ASME) **55,** 569-572 (1933).

[27] L. Kogut, and I. Etsion, Elastic-plastic contact analysis of a sphere and a rigid flat, ASME J. Appl. Mech. **69,** 657-662 (2002). http://dx.doi.org/10.1115/1.1490373

[28] K. Nakajima, H. Yamaguchi, J. –C. Lee, and M. Kageshima, Nanorheology of polymer blends investigated by atomic force microscopy, Jpn. J. Appl. Phys. **36,** 3850-3854 (1997). http://dx.doi.org/10.1143/JJAP.36.3850

[29] H. M. Lee and O. O. Park, Rheology and dynamics of immiscible polymer blends, J. Rheology **38,** 1405-1425 (1994). http://dx.doi.org/10.1122/1.550551

Appendix: Further consideration of particle-tip interaction

The purpose of Sec. 4.2 is to understand and control particle-tip deformation as much as possible during AFM measurement of PSL particle sizes. This is necessary in order to decouple particle-tip interaction from particle-substrate deformation. Our position is that separate estimates of these uncertainty contributions is not possible without additional information or assumptions. We present some relevant measurement data and novel analysis below. Relying on the latter approach, Garnaes obtained estimates for the PSL compressibility terms δ_{PT} and δ_{PS} by assuming elastic deformation, relying on earlier work in Ref. [17]. Plastic deformation was not considered because "…a possible plastic deformation on a nanoscale is not assessed as it has not been thoroughly analyzed in the literature." Misumi employed the elastic model and, by making the additional assumption of zero particle-tip deformation, $\delta_{PT} = 0$, noted this required the use of a two-part thin film - bulk Young's modulus to fit the data. This assumption was motivated by previous studies on the role of the glass transition temperature, T_g, on surface mechanical properties of polymer thin films [22, 23]. According to these ideas and the fact that T_g for polystyrene is about 100 °C, this assumption suggests that a thin-film layer thickness of 2.3 nm would form on the PSL particle surface.

This layer would be sufficient for viscoelastic effects to appear. If we look more closely at Ref. [23], we find that this article connects plastic deformation of polystyrene to a glass-to-rubber transition under AFM tapping mode conditions. In fact, we observe a similar material flow in the front-to-back scanning direction of the asymmetric AFM probe in the case of PSL particles. Such observations are simply inconsistent with a purely elastic deformation model for AFM tapping-mode imaging of compressible materials.

Tamayo & Garcia [24] have discussed the complexity of AFM probe interaction with deformable polymer samples in tapping mode. Deformable in this case is defined by a Young's modulus of $E < 10$ GPa. An interesting point of this work is that it establishes an inverse relationship between contact time and average force for an oscillating tip in close proximity to a surface. Viscous effects were shown to substantially decrease the hardness of the tapping force below a relaxation frequency $w_V = E/\eta$, where E is the Young's modulus and η is the viscosity. Note that the effective range of this parameter depends on both sample and cantilever properties. For polystyrene with $E = 3.3$ GPa and $\eta = 10^3 – 10^4$ Pa·s, a tapping mode probe with an average cantilever resonance frequency of $f_o = 300$ kHz is within this relaxation frequency range. In this case, interaction stiffness increases. On the other hand, the use of an AFM cantilever with a much lower f_o would be subject to viscoelastic forces as well as exciting higher-order cantilever modes. This compromises stability of the electromechanical system making optimal measurements via the set point voltage difficult to set up and maintain during long periods of data acquisition. In addition to the contact time -- or the applied force during tapping mode operation -- the reduced radius, $R_{red}^{-1} = (1/R_{tip} + 1/R_{part})^{-1}$, must be considered in the total load on the nanoparticle. Then, a sharp tip with a radius of 7 nm spends only a quarter of the time tapping at each location than one of twice the radius. Counterintuitively, a blunt tip produces relatively greater deformation than a sharp one under tapping mode imaging conditions.

Rather different elastic and plastic responses of the PSL particles to the tapping load may then appear depending on experimental conditions and the choice of contact mechanical model. We make this clear by acquiring PSL deformation data with two different set-point lowering sequences which we refer to as large step and small step sequences: A graph of apparent height vs. set point voltage for a sequence A_{set} → A' → A"… is presented in Fig. A1a. In this case, the set point voltage is decreased by *large* steps, i.e., $\Delta A = 0.2$ V. Data for six individual PSLs are plotted with their initial height, h_o, indicated on the right hand side of the graph. Deformation increases linearly with decreasing set point voltage. Smaller particles

of the same particle material deform to a greater extent than larger particles. This behavior, attributable to the reduced radius effect noted above, is observed consistently for measurements of this kind.

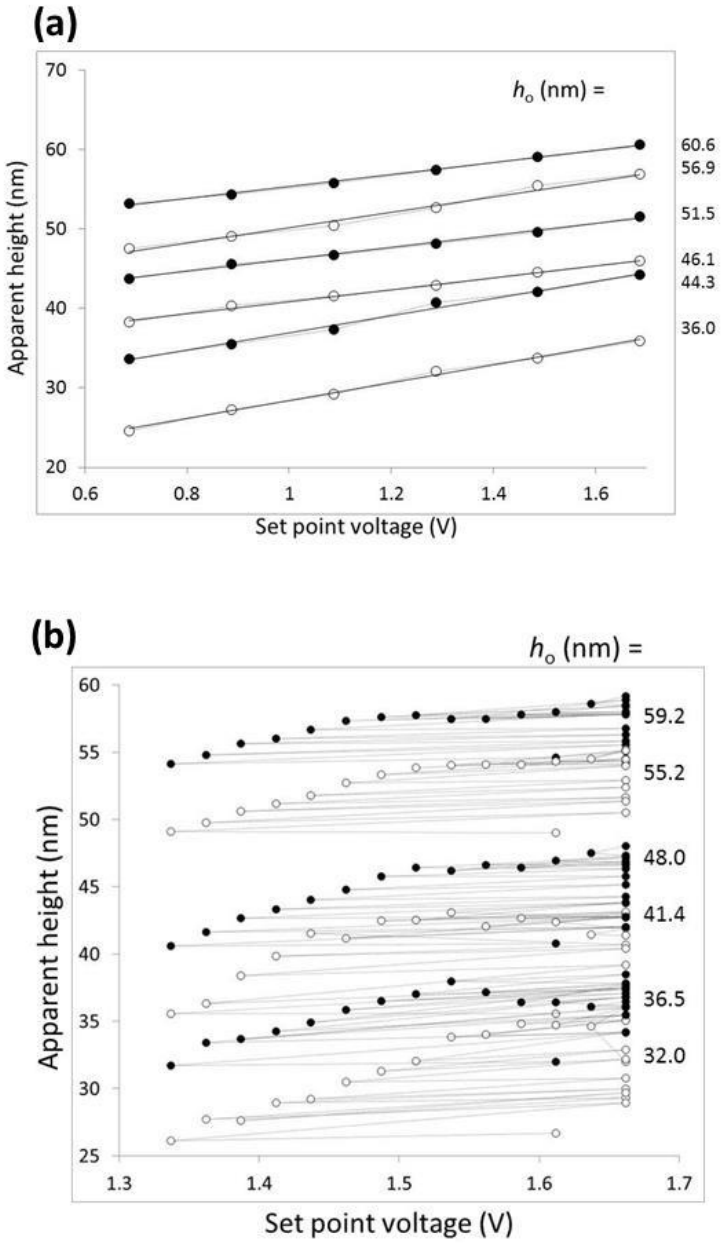

Fig. A1. Apparent height vs set point voltage for (a) large, ΔV = 0.2 V, and (b) small, ΔV = 0.025 V, decreases of the set point voltage. Measurement sequences for six individual PSLs are shown in each panel. The initially measured particle height is indicated on the right hand side of the figure.

Figure A1b presents apparent height vs. set point voltage data, but for a sequence $A_{set} \rightarrow A' \rightarrow A_{set} \rightarrow A''$… in which the set-point voltage decreases by *small steps*, i.e., $\Delta A = 0.025$ V. The appearance of these small step curves resembles the conceptual and empirical results presented earlier in Fig. 6. The essential point is that plastic material response to large decreases in set point voltage, Fig. A1a, should not be used to infer anything about relatively small elastic-plastic interactions, Fig. A1b. It is precisely such small excursions, caused by electromechanical drift or changes in probe shape, which are responsible for the time-dependent uncertainty associated with δ_{PT}.

In contrast, Ref. [7] analyzed peak-force AFM data for PSL nanoparticles using an elastic-plastic model due to Jackson & Green [25]. Their data exhibits a linear response which is evidently very similar to that shown in Fig. A1a. They concluded that AFM in general operates in a regime where large plastic deformation of PSLs is inevitable. Indeed, they suggested that, δ_{PT} may be considerably larger than δ_{PS}.

This conclusion is at variance with the measurements and analysis we have presented in this work. To attempt a resolution of the issue, we recall that, according to the conclusions of Ref. [24] cited above, viscoelastic effects may be more prominent at lower frequencies than higher ones. Since peak-force is a nonresonant, low-frequency mode compared with tapping mode, viscoelastic effects ought to play a more prominent role in peak-force deformation. In particular, it is inappropriate to extrapolate compressibility results obtained from those presented in Fig. A1a -- or, for that matter, peak-force imaging -- to tapping mode imaging conditions well above the yield point indicated in Fig. 6. This becomes more apparent by averaging the data sets in Fig. A1and replotting them in Fig. A2 in terms of an applied force appropriate for each regime.

The large-step data in Fig. A1a, for example, can be readily interpreted on the basis of the Abbott-Firestone [26] approximation for the strongly plastic regime. This model is used to transform AFM parameters, Fig. A2a, into a standard deformation vs force representation, shown in Fig. A2b. (F_{AF} in the figure refers to the applied force calculated from the Abbott-Firestone model). We can then interpret the linear deformation regime as follows: Stiffness increases under tapping-mode conditions and tapping harder leads to deeper penetration of the plastic region into the polymer material according to Ref. [24]. Since the tapping frequency in our measurements is close to, or exceeds, the relaxation frequency of PSL [28, 29], the compounding of strong plasticity is consistent with theories from both contact mechanics and AFM tapping mode.

On the other hand, calculations based on the work of Kogut & Etsion [27] predict the modification depth for the elastic-plastic situation, Fig. A1b: As before, AFM parameters in Fig. A2a are transformed into a standard deformation vs force representation in Fig. A2b. (F_{KE} in the figure refers to the applied force calculated from the Kogut & Etsion model). Elastic-plastic behavior for small applied loads is evidently sublinear and is given by a deformation vs force relationship, $d \propto F^{0.71}$.

A comparison of these results leads to the conclusion that the interaction of the probe tip with a PSL particle induces different non-additive material responses into the polymer material depending on the regime. A given applied force of 2 nN, say, in Fig. A2b, delivered in a single, direct step produces substantially greater deformation, almost a factor of 5 greater, than from the load deposited by a succession of much smaller ones, even if this sequence eventually reaches 2 nN. This seems to be a consequence of the fact, emphasized in Ref. [25], that hardness, $H = 2.8\ S_y$, and therefore yield strength are not constant. Thus the ratio of the yield strength to elastic modulus, S_y/E, evolves through the course of elastic-plastic deformation through an increase in material stiffness.

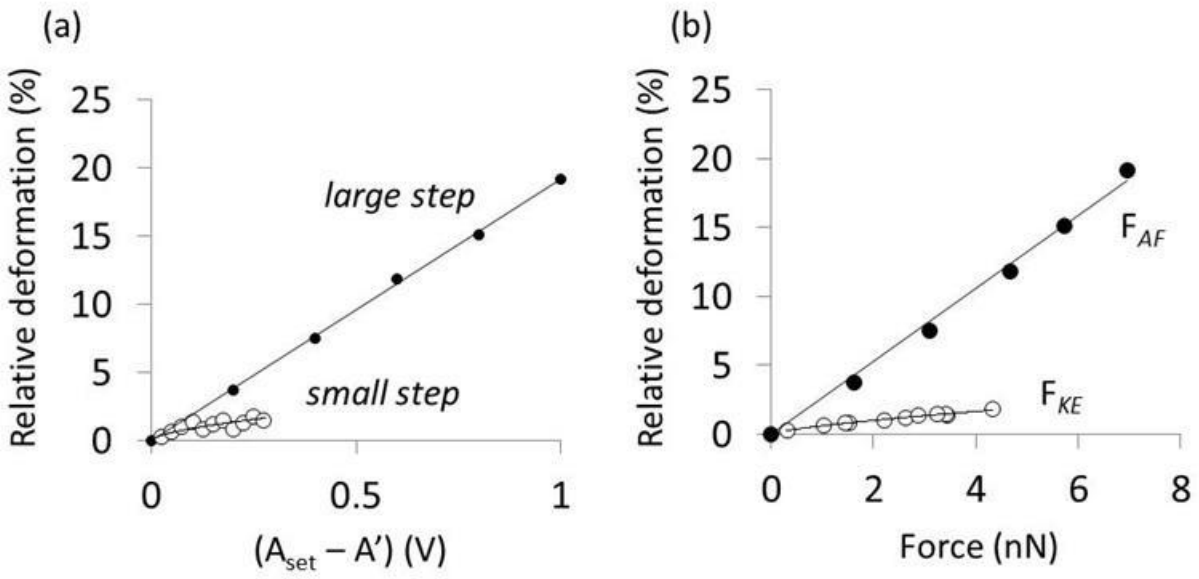

Fig. A2. Conversion of apparent height vs. set point data into a normalized deformation vs. force plot for the large- and small-step sequences in Fig. A2. The linear increase under strong plasticity follows the same behavior obtained for peak-force data in Ref. [7].